Nuclear Instruments and Methods in Physics Research A 1057 (2023) 168729

Contents lists available at ScienceDirect

Nuclear Inst. and Methods in Physics Research, A

journal homepage: www.elsevier.com/locate/nima

Research on an active control method of double crystal monochromator with disturbance observer

Yang Bai [a,b,c,d], Xuepeng Gong [a,b,c,d,*], Qipeng Lu [a,b,c,d,**], Shengchi Li [a,b,c,d], Yuan Song [a,b,c,d], Zhongqi Peng [a,b,c,d], Zhen Zhang [a,b,c,d]

[a] Changchun Institute of Optics, Fine Mechanics and Physics, Chinese Academy of Sciences, Changchun, 130033, China
[b] University of Chinese Academy of Sciences, Beijing, 100049, China
[c] State Key Laboratory of Applied Optics, Changchun Institute of Optics, Fine Mechanics and Physics, Chinese Academy of Sciences, Changchun, 130033, China
[d] Key Laboratory of Optical System Advanced Manufacturing Technology, Chinese Academy of Sciences, Changchun, 130033, China

ARTICLE INFO

Keywords:
Double crystal monochromator
Disturbance observer
Notch filter
Fourth generation synchrotron light source

ABSTRACT

The double crystal monochromator (DCM) is the core equipment of high flux and high monochromatic light on the synchrotron beamline, which directly affects the performance of the synchrotron hard X-ray beamline in terms of stability. To meet the requirements for the stability of the nano-radian magnitude of the DCM for the 4th-generation synchrotron light source, this paper presents a method to suppress the primary resonance of the system using an integral lead compensation notch filter and eliminate the higher-order positive and negative resonance peaks with a dual second-order notch filter. The bandwidth of the DCM system is enhanced to meet the system speed requirements. Meanwhile, the mechanical coupling is considered equivalent to the system's internal disturbance. The disturbance observer is designed to ensure the stability and dynamic performance of the DCM system. The simulation results show that after correction by the integral lead compensation notch filter and the dual second-order notch filter, the system bandwidth can reach 308Hz while maintaining a phase margin of approximately 25°. Furthermore, the stability of DCM can reach an RMS of 0.139 nrad, 16.610 nrad, and 1.431 nm in the Pitch, Roll, and Gap direction, respectively, with the help of a disturbance observer. The paper proposes a method to develop stable DCMs in 4th-generation synchrotron radiation facilities while improving the X-ray beamline performance.

1. Introduction

The scientific research platform based on synchrotron X-ray provides advanced experimental technology means for many disciplines such as physics, chemistry, life science, material science, information science, energy, and environmental science, and has extensive applications in biopharmaceuticals, petrochemicals, microelectronics, and other fields, which is an irreplaceable new light source for high-level scientific experiments [1]. The new generation synchrotron light sources are diffraction-limited sources and free electron lasers with high coherence and high brilliance, with extremely high coherence and very small focusing optical properties, enabling in situ, dynamic, and high-resolution scientific experiments, providing unprecedented opportunities for fundamental scientific research [2–5]. The DCMs in the synchrotron light source separate X-rays of specific wavelengths from the continuous synchrotron radiation spectrum. In addition, the DCMs can be controlled by an external control system to achieve precise adjustment of the attitude of the double crystal to change the wavelength of the output synchrotron light to obtain different energy beamlines required in practical research, which is a high performance, mature technology, and simple and reasonable structure and widely application monochromator [6]. For the hard X-ray beamline of the synchrotron light source, the disturbance caused by the liquid nitrogen cooling system and other factors leads to a change in the relative position of the double crystal, which severely affects the relative stability of the double crystal. Consequently, the beam spot quality required for scientific experiments is decreased substantially [7–10].

In general, optimizing the structure of the liquid nitrogen cooling system is the standard method for improving the stability of DCMs. Yamazaki et al. (2013) designed a low-vibration flexible tube to stabilize

* Corresponding author. Changchun Institute of Optics, Fine Mechanics and Physics, Chinese Academy of Sciences, Changchun, 130033, China.
** Corresponding author. Changchun Institute of Optics, Fine Mechanics and Physics, Chinese Academy of Sciences, Changchun, 130033, China.
E-mail addresses: gongxuepeng120@foxmail.com (X. Gong), luqipeng@126.com (Q. Lu).

https://doi.org/10.1016/j.nima.2023.168729
Received 18 July 2023; Received in revised form 2 September 2023; Accepted 25 September 2023
Available online 26 September 2023

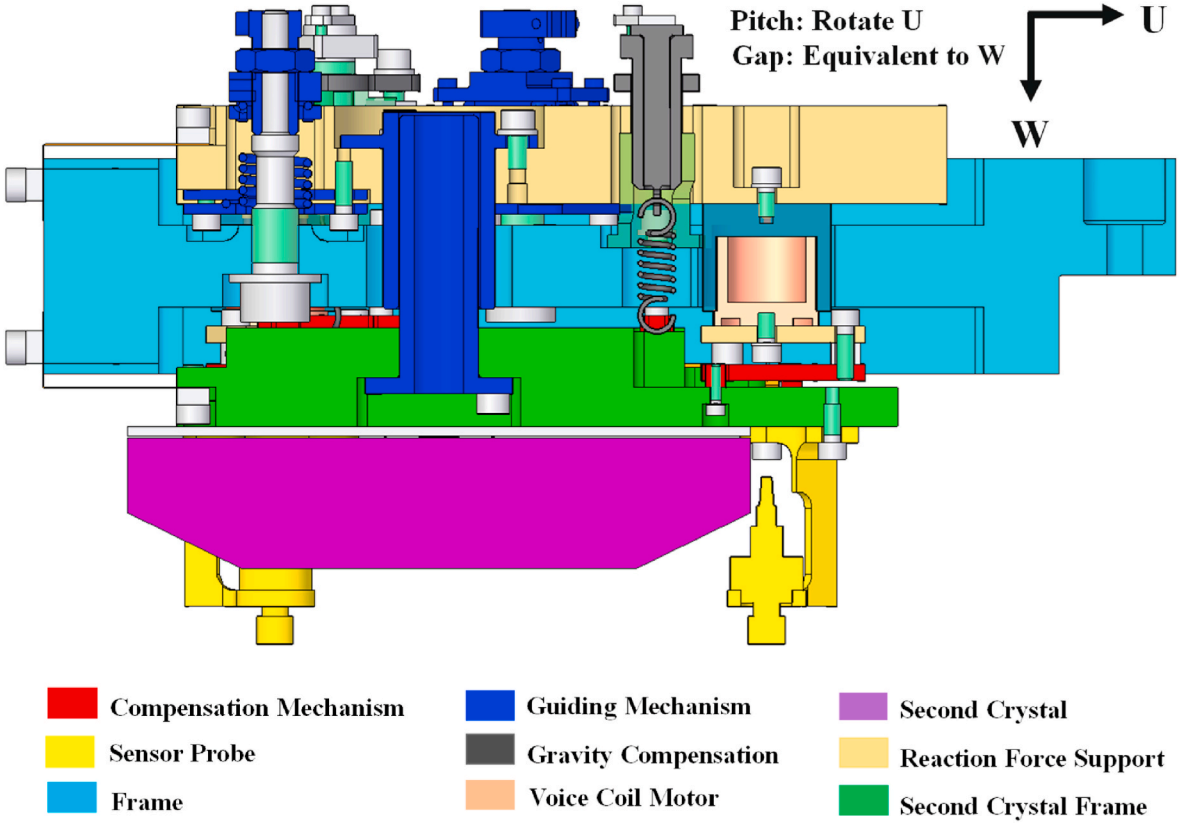

Fig. 1. Stability adjustment mechanism for the DCM's second crystal.

the coolant flow by covering the corrugation of the flexible tube with alumina fiber fabric, thus ensuring the stability of the crystal monochromator and reducing the vibration deflection angle between the crystals from 1″ to 0.15″, and achieving 230 nm size focus by projecting the light source onto the focal plane [11]. The Spring-8 (2019) source upgraded the cooling circuit of the second crystal, and the crystal's stability can be theoretically improved to 50 nrad [12]. SSRF designed an indirect cooling method to enhance the structure of the flexible hinge of the second crystal fine adjustment mechanism while reducing the weight of the associated structural components and effectively improving the crystal parallelism [13]; On the other hand, the angular stability of the exit beam was improved by the design of the second crystal clamping mechanism, the optimized layout of the liquid nitrogen line, and the upgrade of the insulation and temperature stabilization system [7]. Qin (2022) et al. designed a novel cradle-type crystal adjustment mechanism based on cross flexure, which achieved a relatively Pitch vibration of 31.5 nard (RMS) with good stability in the 0.1 ~ 100 Hz bandwidth of the monochromator at a liquid nitrogen flow rate of 2.4 L/min [14]. As fourth-generation synchrotron light sources with low emittance (≤100 p.m. rad) continue to emerge worldwide, extremely demanding requirements are imposed on the stability index of DCMs. The active control method to solve the DCM stability problem has attracted much attention from many researchers. Geraldes et al. proposed a novel approach to the design of DCM based on the mechatronics concept, the dynamic structure of the DCM is derived from semiconductor manufacturing equipment, and the prototype of DCM is predicted to achieve closed-loop bandwidth of more than 200 Hz by a solution based on voice coil motor drivers and balanced masses [15–17]. Bai et al. simulated the application of the adaptive filtering algorithm and derivatives of the algorithm to the stability problem of DCM [18–20].

In this paper, we present the design of a three-degree-of-freedom stability adjustment mechanism for the DCM's second crystal related to the Sirius light source high dynamics crystal monochromator [16], as depicted in Fig. 1. Fig. 2 illustrates the load-bearing mechanism of the second crystal of the DCM. In this paper, ANSYS/Workbench applies the sweep excitation (size 1 N, frequency range 0~1000Hz) to the X/Y/Z points, respectively. The least squares system identification method derives the transfer function for the X/Y/Z three-point system and the coupled transfer function. Secondly, a notch filter is designed based on the system's root locus method to eliminate the primary resonance. A dual second-order filter is then designed to suppress the high-order positive and negative resonance peaks, improving the bandwidth of the DCM system to meet the speed requirements. The integral lead compensation controller is designed to ensure steady-state accuracy, allowing the system bandwidth to reach over 300Hz with a phase margin of approximately 25°. To ensure the stability and disturbance suppression ability of the DCM system, a disturbance observer is designed while considering external liquid nitrogen interference, mechanical coupling factor disturbances, and sensor noise interference. The tracking ability of the system under 50nrad/300Hz sinusoidal input is verified based on Simulink, and the lead compensation controller compensates the phase of the system to improve the tracking accuracy of the system.

2. System modeling and controller design

2.1. System modeling

It is known from Figs. 1 and 2 that the stability adjustment mechanism of the DCM is a 3-input and 3-output motion system for the second crystal. Typically, the 3-input, 3-output system is transformed into three distinct single-input, single-output (SISO) systems. Each logic axis is independently controlled by its own controller. The system's primary control block diagram is depicted in Fig. 3, based on the description above. After receiving the current position from the stability adjustment

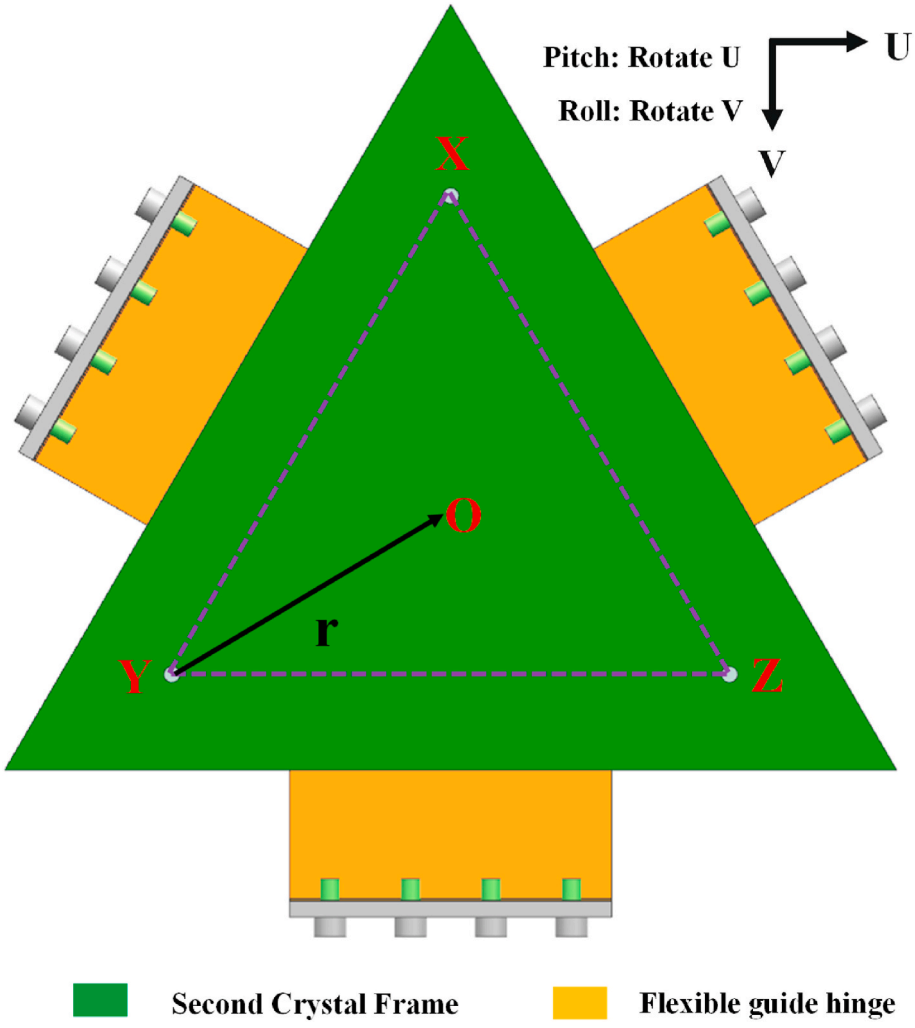

Fig. 2. Schematic diagram of the second crystal-bearing mechanism of DCM.

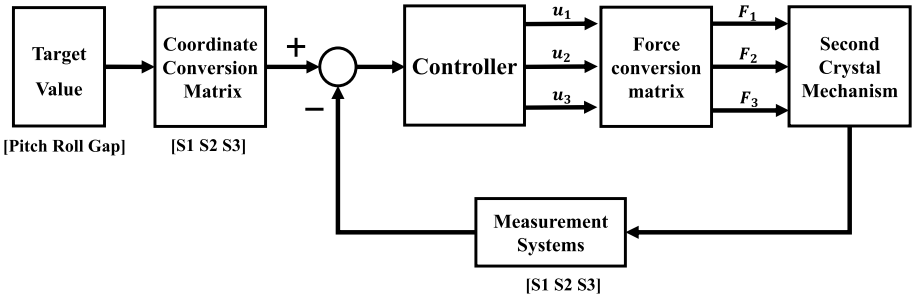

Fig. 3. Block diagram of the primary control principle of the system.

mechanism, the position [Pitch; Roll; Gap] is converted to the motion coordinates of the 3-axes physical axes [S1; S2; S3] through coordinate conversion (S1, S2, and S3 correspond to the displacements of points X, Y, and Z in the vertical direction). Based on the deviation signal, the controller calculates control quantities. The motion coordinates of each physical axis are then transformed into the actual driving force of each voice coil motor through the force conversion matrix. Based on Fig. 2, equation (1) shows how the motion axis of the stability adjustment mechanism can convert to the logic axis:

$$\left\{\begin{array}{l} \text{Gap} = \dfrac{\text{S1} + \text{S2} + \text{S3}}{3} \\ \text{Pitch} = \dfrac{-2\text{S1} + \text{S2} + \text{S3}}{3\text{r}} \\ \text{Roll} = \dfrac{-\text{S2} + \text{S3}}{\sqrt{3}\text{r}} \end{array}\right\} \tag{1}$$

The physical axes are labeled S1, S2, and S3; the logical axes are labeled Gap, Pitch, and Roll. Where S1, S2, and S3 correspond to the displacements of points X, Y, and Z in the vertical direction (The vertical direction is the direction of the coordinate axis W in Fig. 1); The meaning of the variable "r" in terms of physical significance can be found in Fig. 2.

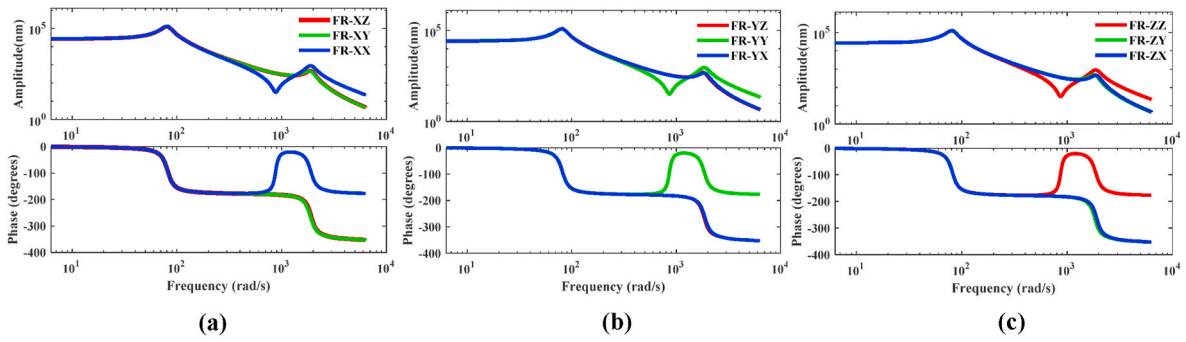

Fig. 4. Frequency response of X, Y, and Z points of the second crystal active control mechanism. (a) X-point excitation (b) Y-point excitation (c) Z-point excitation.

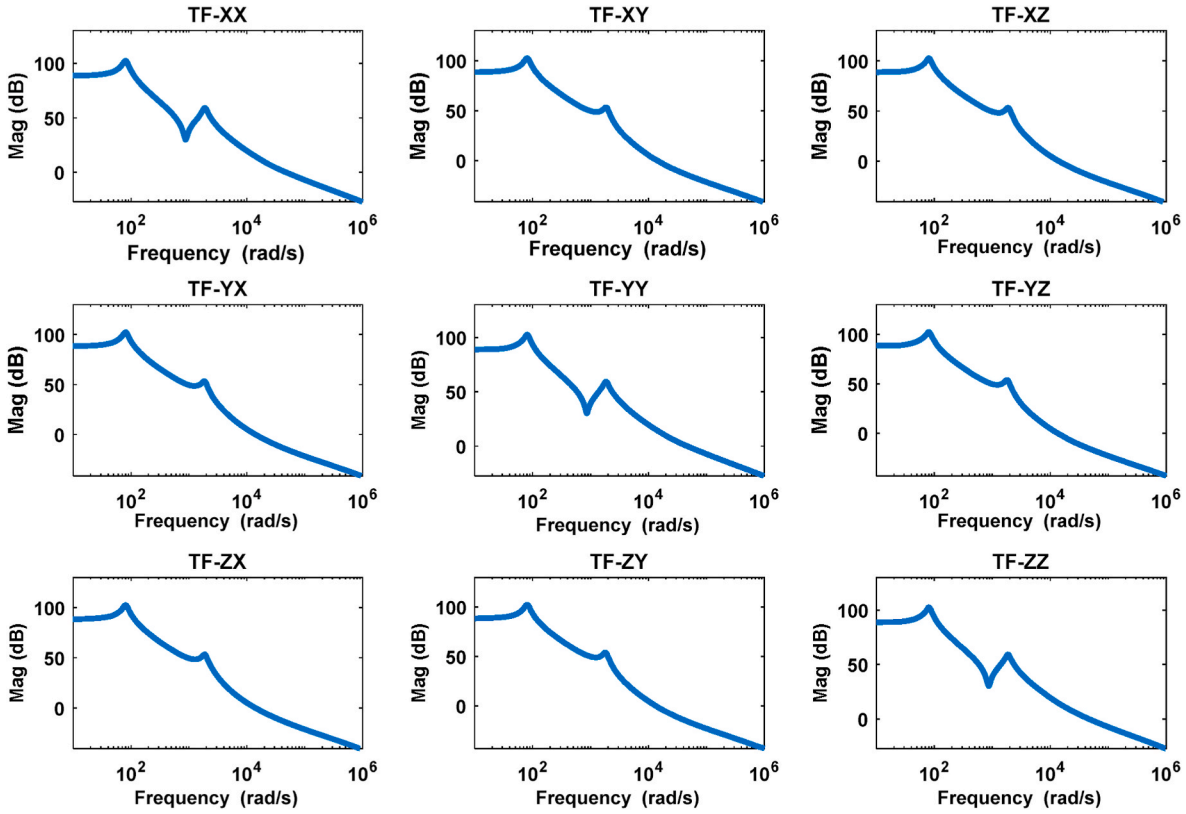

Fig. 5. Bode diagram of the system transfer function.

Equation (1) is written in matrix form as

$$\begin{bmatrix} \text{Gap} \\ \text{Pitch} \\ \text{Roll} \end{bmatrix} = \begin{bmatrix} \frac{1}{3} & \frac{1}{3} & \frac{1}{3} \\ \frac{-2}{3r} & \frac{1}{3r} & \frac{1}{3r} \\ 0 & \frac{-1}{\sqrt{3}r} & \frac{1}{\sqrt{3}r} \end{bmatrix} \begin{bmatrix} S1 \\ S2 \\ S3 \end{bmatrix} \tag{2}$$

The relationship between the forces, moments, and thrust forces in the stability adjustment mechanism 's three degrees of freedom at X, Y, and Z is displayed in (3):

$$\begin{cases} F_{Gap} = F_X + F_Y + F_Z \\ M_{Pitch} = \left(F_X - \frac{F_Y}{2} - \frac{F_Z}{2}\right) \times r \\ M_{Roll} = (F_Y - F_Z) \times \frac{\sqrt{3}r}{2} \end{cases} \tag{3}$$

The force F_{Gap} generates degrees of freedom in the Gap direction. M_{Pitch} is the moment that causes the system to create space in the Pitch direction. M_{Roll} is the moment that causes the system to generate roll space degrees. F_i is the force at point i,(i = X, Y, Z). Equation (3) is written in matrix form as

$$\begin{bmatrix} F_{Gap} \\ M_{Pitch} \\ M_{Roll} \end{bmatrix} = \begin{bmatrix} 1 & 1 & 1 \\ r & \frac{-r}{2} & \frac{-r}{2} \\ 0 & \frac{\sqrt{3}r}{2} & \frac{-\sqrt{3}r}{2} \end{bmatrix} \begin{bmatrix} F_X \\ F_Y \\ F_Z \end{bmatrix} \tag{4}$$

Based on the principles of system dynamics, we can establish the following equation for the stability adjustment mechanism:

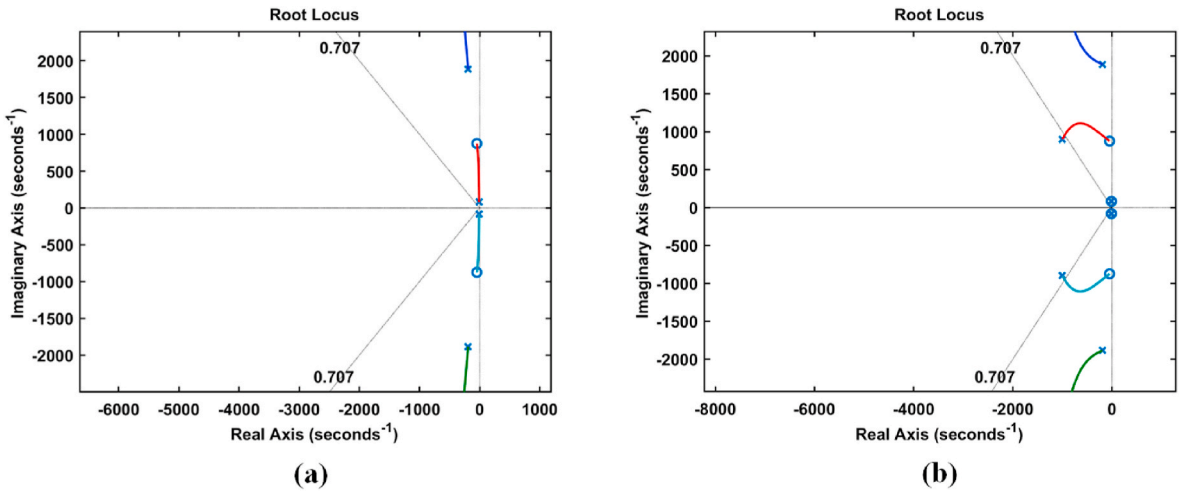

Fig. 6. The root locus diagram of the TF-XX system. (a) Before correction (b) After correction.

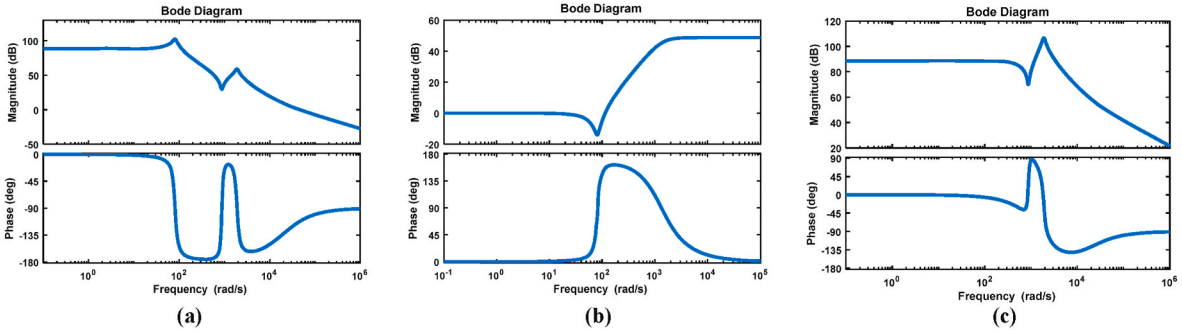

Fig. 7. Bode diagram for eliminating primary harmonic. (a) Bode diagram for TF-XX system. (b) Bode diagram for Notch Filter. (c) Bode diagram for a system with Notch Filter.

$$\begin{bmatrix} m_{Gap} & 0 & 0 \\ 0 & J_{Pitch} & 0 \\ 0 & 0 & J_{Roll} \end{bmatrix} \begin{bmatrix} \ddot{Gap} \\ \ddot{Pitch} \\ \ddot{Roll} \end{bmatrix} + \begin{bmatrix} C_{Gap} & 0 & 0 \\ 0 & C_{Pitch} & 0 \\ 0 & 0 & C_{Roll} \end{bmatrix} \begin{bmatrix} \dot{Gap} \\ \dot{Pitch} \\ \dot{Roll} \end{bmatrix} + \begin{bmatrix} K_{Gap} & 0 & 0 \\ 0 & K_{Pitch} & 0 \\ 0 & 0 & K_{Roll} \end{bmatrix} \begin{bmatrix} Gap \\ Pitch \\ Roll \end{bmatrix} = \begin{bmatrix} F_{Gap} \\ M_{Pitch} \\ M_{Roll} \end{bmatrix} \tag{5}$$

Where m represents equivalent mass, J represents equivalent rotational inertia, C represents equivalent damping, and K represents equivalent stiffness. By plugging equations (3) and (4) into equation (5), we get:

The letter "f" represents the disturbance that has an equivalent value.

This paper uses the least squares method to identify system parameters for an accurate model and excellent control of the stability adjustment mechanism. Based on the dynamics analysis method of ANSYS/Workbench, harmonic signals with a linear increase in frequency from 0 Hz to 1000 Hz and an amplitude of 1 N are selected as the inputs of X, Y, Z in Fig. 2. (The Y/Z input is held at zero when the X point is input; the X/Z input is held at zero when the Y point is input; and the X/Y input is held at zero when the Z point is input.). The frequency response function of the system is depicted in Fig. 4. In Fig. 4(a), FR-XX is the frequency response at point X when the excitation is applied at point X; FR-XY is the frequency response at point Y when the excitation

$$\begin{bmatrix} m_{Gap} & 0 & 0 \\ 0 & J_{Pitch} & 0 \\ 0 & 0 & J_{Roll} \end{bmatrix} \begin{bmatrix} \frac{1}{3} & \frac{1}{3} & \frac{1}{3} \\ \frac{-2}{3r} & \frac{1}{3r} & \frac{1}{3r} \\ 0 & \frac{-1}{\sqrt{3}r} & \frac{1}{\sqrt{3}r} \end{bmatrix} \begin{bmatrix} \ddot{S}1 \\ \ddot{S}2 \\ \ddot{S}3 \end{bmatrix} + \begin{bmatrix} C_{Gap} & 0 & 0 \\ 0 & C_{Pitch} & 0 \\ 0 & 0 & C_{Roll} \end{bmatrix} \begin{bmatrix} \frac{1}{3} & \frac{1}{3} & \frac{1}{3} \\ \frac{-2}{3r} & \frac{1}{3r} & \frac{1}{3r} \\ 0 & \frac{-1}{\sqrt{3}r} & \frac{1}{\sqrt{3}r} \end{bmatrix} \begin{bmatrix} \dot{S}1 \\ \dot{S}2 \\ \dot{S}3 \end{bmatrix}$$
$$+ \begin{bmatrix} K_{Gap} & 0 & 0 \\ 0 & K_{Pitch} & 0 \\ 0 & 0 & K_{Roll} \end{bmatrix} \begin{bmatrix} \frac{1}{3} & \frac{1}{3} & \frac{1}{3} \\ \frac{-2}{3r} & \frac{1}{3r} & \frac{1}{3r} \\ 0 & \frac{-1}{\sqrt{3}r} & \frac{1}{\sqrt{3}r} \end{bmatrix} \begin{bmatrix} S1 \\ S2 \\ S3 \end{bmatrix} = \begin{bmatrix} 1 & 1 & 1 \\ r & \frac{-r}{2} & \frac{-r}{2} \\ 0 & \frac{\sqrt{3}r}{2} & \frac{-\sqrt{3}r}{2} \end{bmatrix} \begin{bmatrix} F_X + f_1 \\ F_Y + f_2 \\ F_Z + f_3 \end{bmatrix} \tag{6}$$

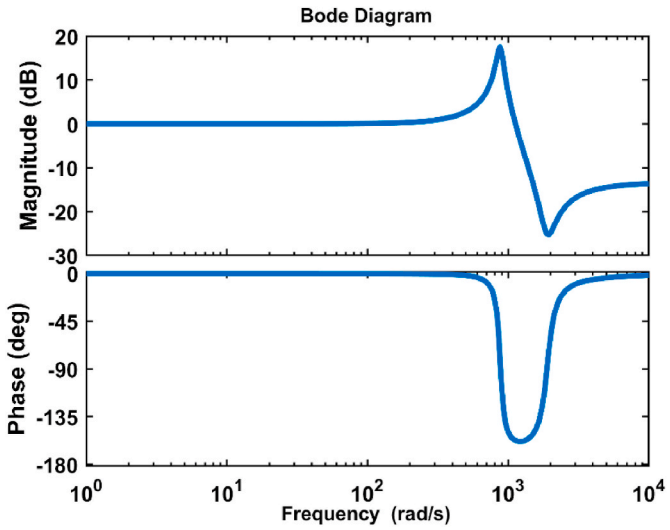

Fig. 8. Bode diagram of Notch Filter based on zero-pole pair cancellation.

is applied at point X; FR-XZ is the frequency response at point Z when the excitation is applied at point X; Fig. 4(b) and (c) are defined in the same way as in Fig. 4(a). Based on the least squares method to identify the system parameters, the system transfer function Bode diagram is obtained as shown in Fig. 5. TF-XX is the transfer function of input X output at point X; TF-XY is the transfer function of input Y output at point X; TF-XZ is the transfer function of input Z output at point X. TF-YY/TF-YX/TF-YZ/TF-ZZ/TF-ZX/TF-ZY are defined in the same way as above.

2.2. Controller design

The active control idea relies on system bandwidth as the primary index for the DCM. If the bandwidth is wide, the system's ability to track is significant. On the other hand, if the bandwidth is too wide, the system's ability to suppress high-frequency disturbances and noise will be reduced. Choosing the appropriate bandwidth is essential in developing a control system for the stability adjustment mechanism. This paper incorporates an appropriate correction link into the system to shape the desired open-loop frequency domain characteristic curve based on the transfer function model identified in 2.1.

According to Fig. 5, TF-XX has a first-order harmonic frequency of approximately 80 rad/s (12 Hz) and a second-order harmonic peak of

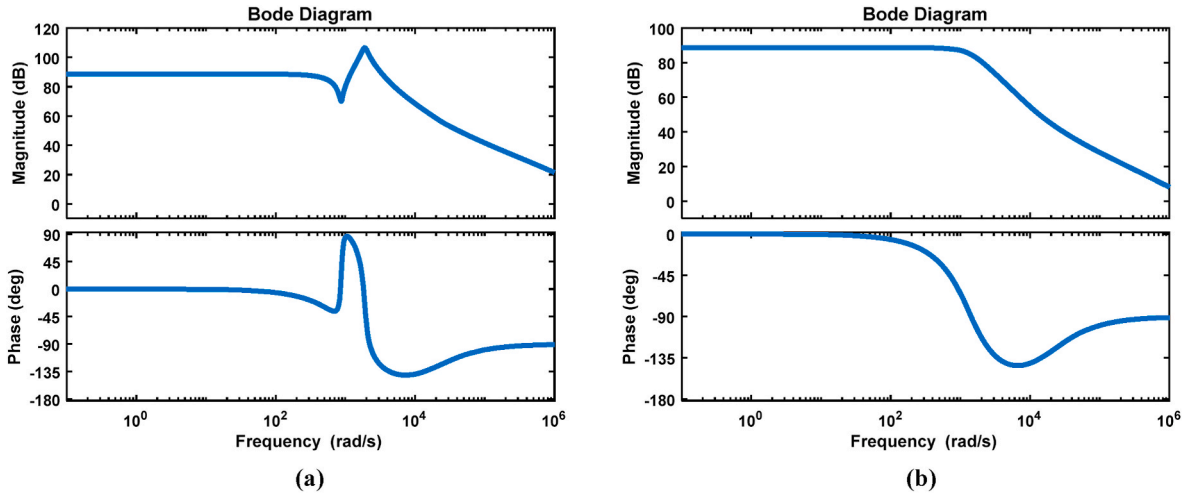

Fig. 9. Bode diagram of eliminating positive and negative harmonics. (a) Bode diagram of the system removing primary harmonics. (b) Bode diagram of the system eliminating positive and negative harmonics.

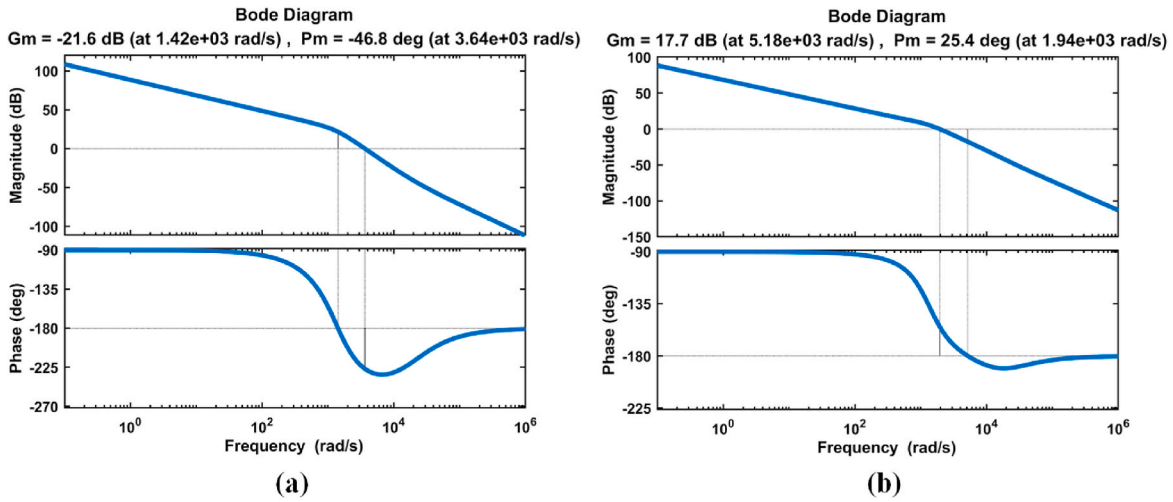

Fig. 10. Bode diagram of integral overcorrection system. (a) Open-loop frequency characteristic curve of the system with the addition of necessary and notch controllers. (b) The open-loop frequency-frequency characteristic curve of the system under the integral lead notch controller.

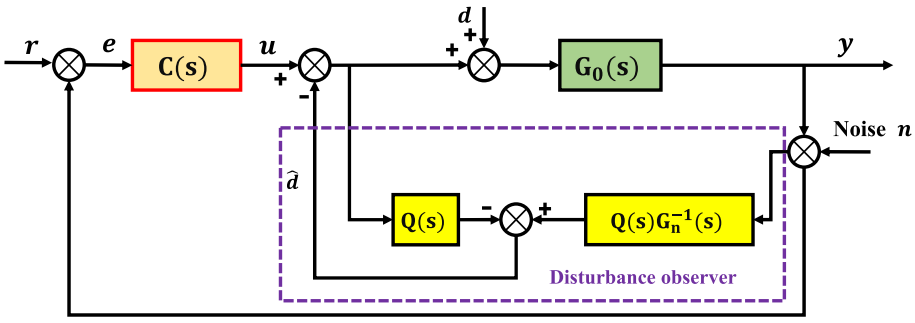

Fig. 11. Typical Disturbance Observer basic schematic.

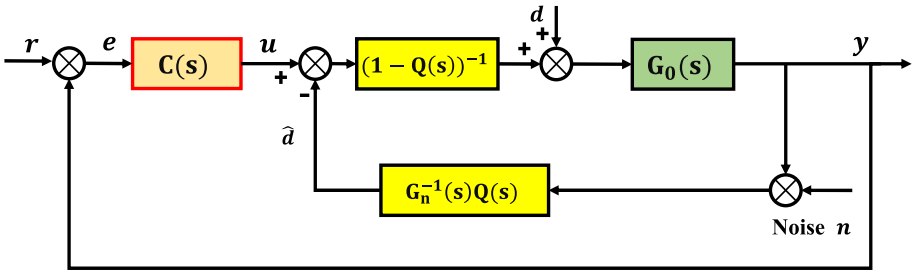

Fig. 12. Disturbance observer equivalent structure diagram.

Table 1
Filter design parameters.

N = 1	$\tau = 0.01$	r = 1
	$\tau = 0.001$	
	$\tau = 0.0001$	
N = 3	$\tau = 0.01$	r = 2
	$\tau = 0.001$	
	$\tau = 0.0001$	

nearly 1876 rad/s (298 Hz). The resonance must be eliminated to meet the open-loop bandwidth requirement of 300Hz. The commonly applied method for primary harmonic oscillation includes velocity feedback, hysteresis correction link, and notch filter. This paper presents a notch filter design that eliminates primary harmonic oscillation using the root locus method. The root locus of the system before adding the notch filter is shown in Fig. 6(a). If the pole of a second-order system is located in a region where the damping ratio is less than 0.707, then the system will have harmonics. The common choke zeros are placed near the target

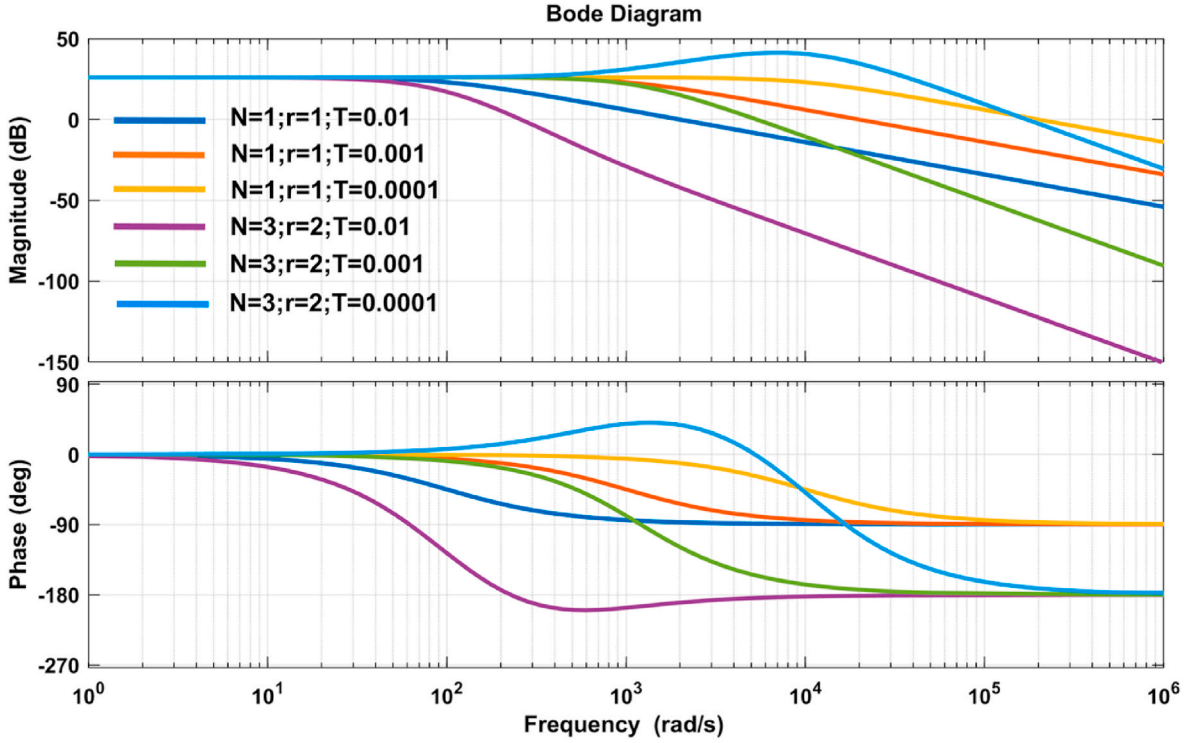

Fig. 13. Low-pass filter Q(s) Bode diagram with different parameters.

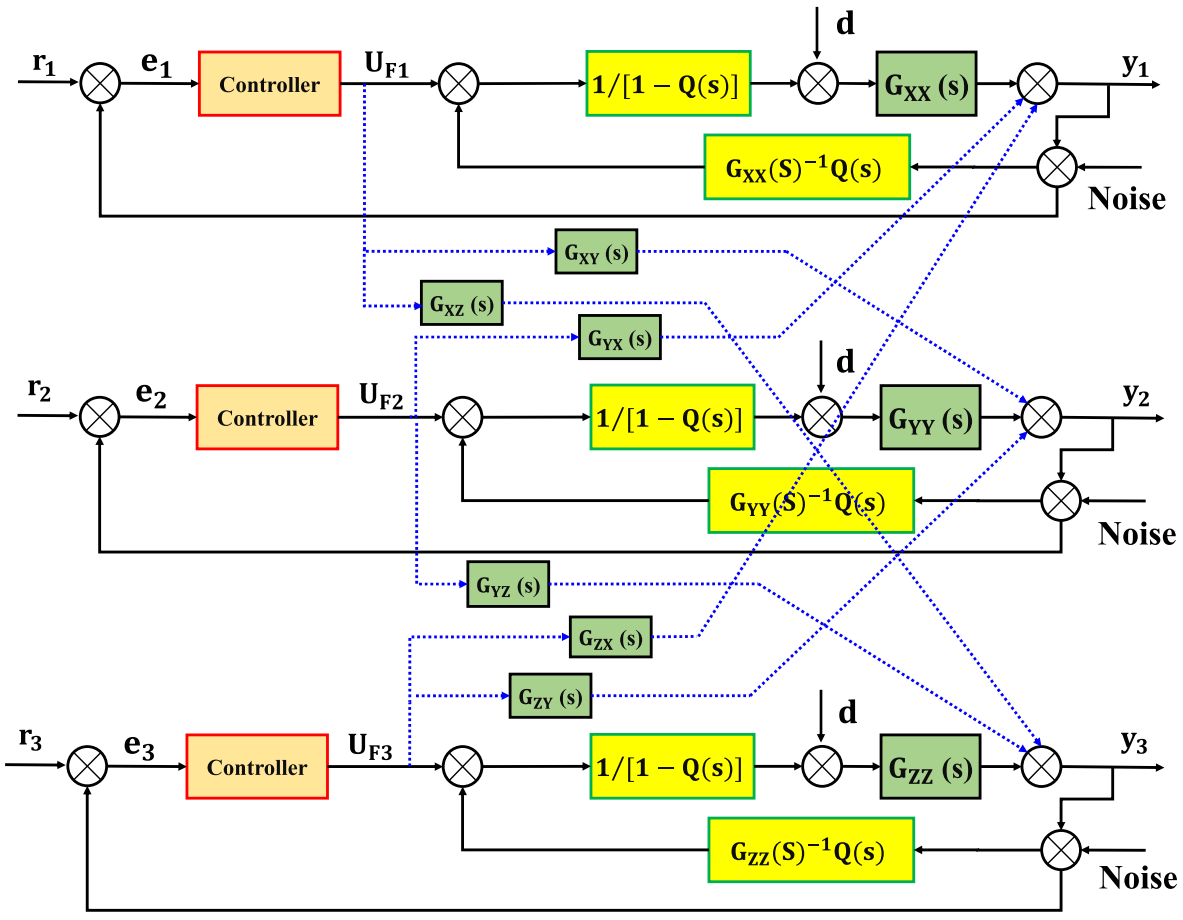

Fig. 14. Basic block diagram of second crystal closed-loop control based on disturbance observer.

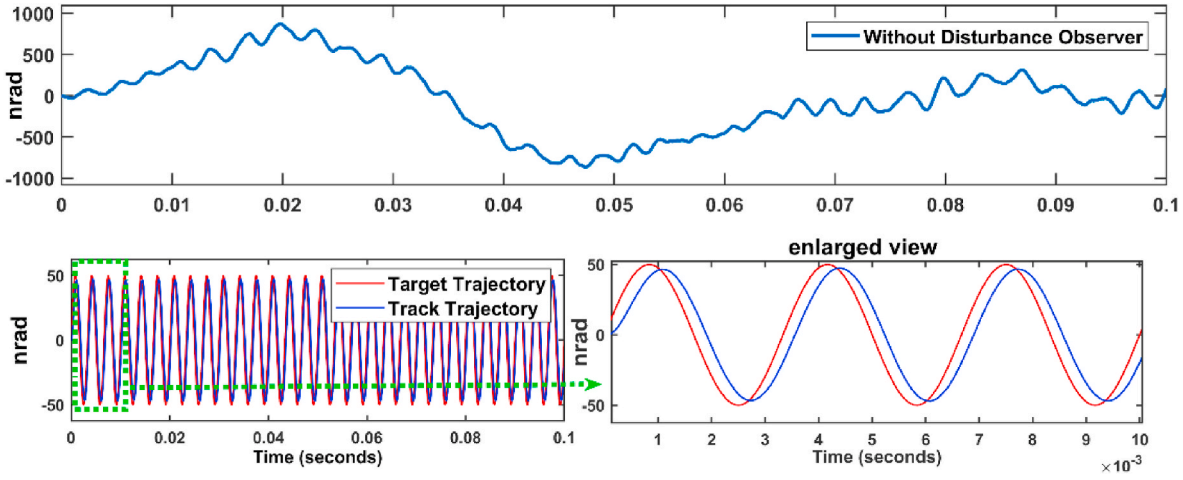

Fig. 15. Tracking effect of system @50nrad/300Hz

pole, followed by the placement of conjugate poles in the region where the damping ratio is greater than 0.707. Currently, the conjugate pole of the newly controlled object is located in an area where the damping ratio is more critical than 0.707. The new controlled object will not have primary harmonics, and the root locus of the system before adding the notch filter is shown in Fig. 6(b). The Bode diagram in Fig. 7(b) shows the notch filter designed using the root locus method. It can increase the phase angle of the system by almost 180° and eliminate system resonance. The Bode diagram of the system after adding the notch filter is shown in Fig. 7(c), and it is evident that the primary harmonic of the open-loop Bode diagram is eliminated. The dual second-order notch filter controller is designed to eliminate high-order positive and negative harmonic peaks near 849 rad/s (135 Hz) and 1876 rad/s (298 Hz). The designed notch filter Bode diagram is shown in Fig. 8, and the corrected Bode diagram of the system is shown in Fig. 9. (a). The root locus method can design a notch filter that eliminates the primary harmonic and provides a lead angle of almost 180, significantly improving system performance. However, after adding the notch filter, since the low-frequency band is relatively flat, the steady-state error cannot be eliminated, and the system robustness is not satisfactory, it is evident that the

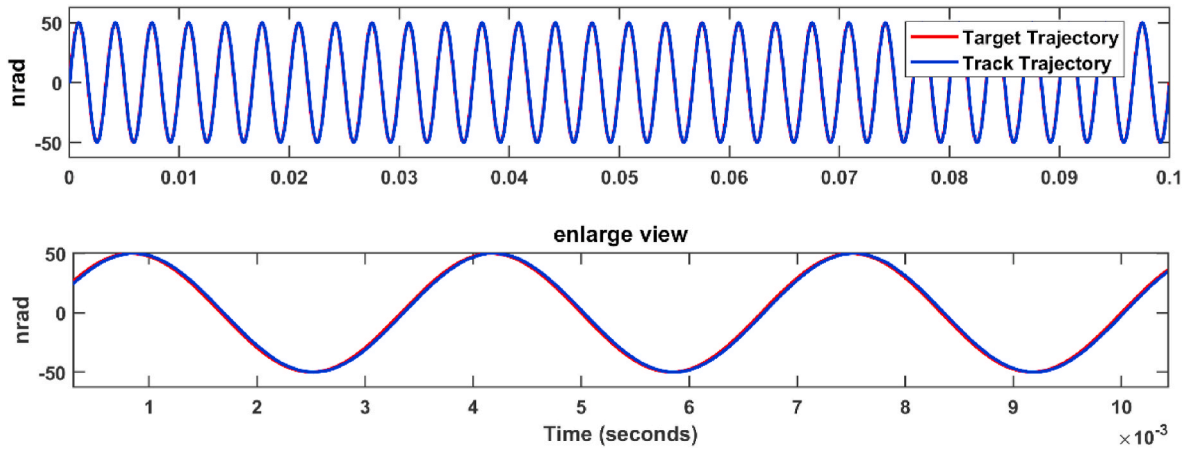

Fig. 16. Tracking effect of the system with phase angle compensation@50nrad/300Hz

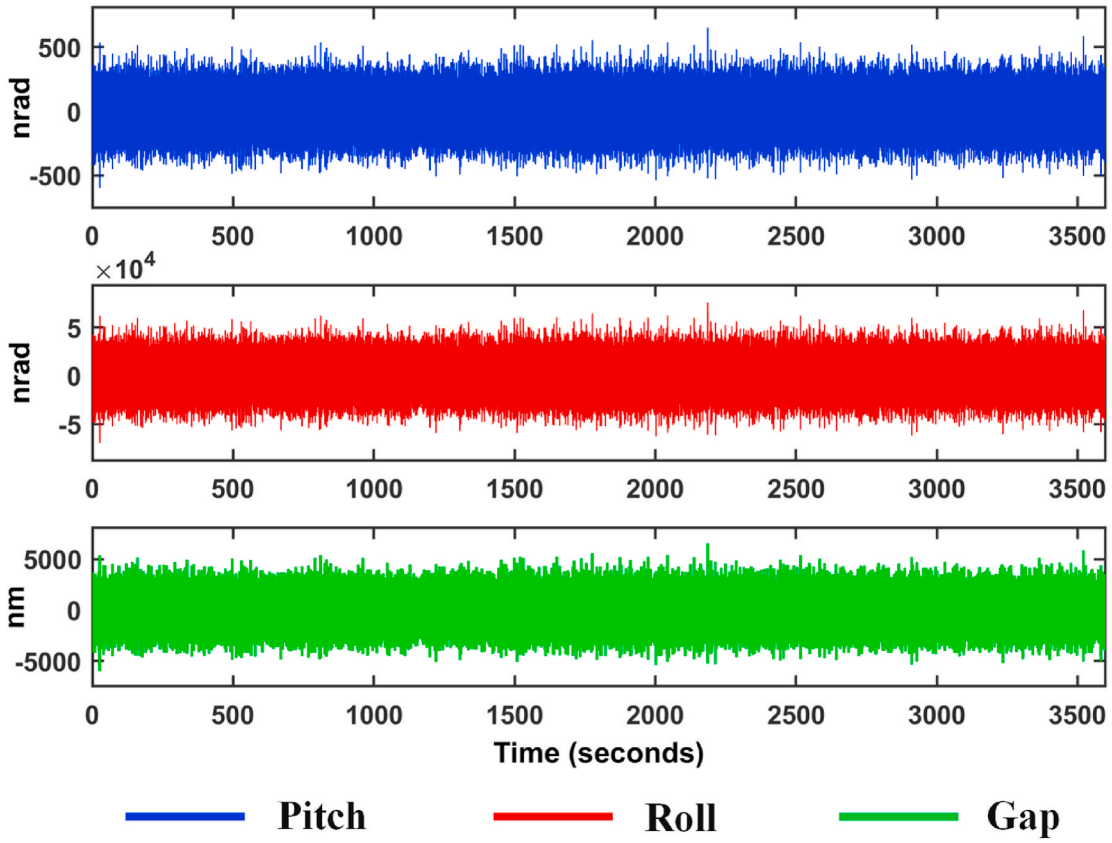

Fig. 17. Stability results for the second crystal without disturbance observer.

system performance still cannot reach the desired index by relying on the notch filter only.

The integration link is required to eliminate steady-state position errors of the system under step input signals for better error reduction. The system's open-loop amplitude-frequency characteristic curve is corrected by adding the integration and proportional links based on the notch filter. The Bode diagram for the corrected system is shown in Fig. 10(a). Since the integration pulls down the phase angle margin of the system, the phase angle margin of the system is relatively small. Thus, to improve the phase angle margin of the system, it is necessary to add another lead compensation link. Fig. 10(b) shows the Bode diagram of the system after the lead correction link is added. Fig. 10(b) shows the system can eliminate primary harmonic, forward and reverse resonance with integral + notch filter + lead compensation controller. This increases system bandwidth to over 300 Hz while ensuring a phase margin of about 25°.

3. Disturbance observer design

Disturbance observers are commonly used in precision servo control, robot control, and numerical control [21,22]. They do not require knowledge of control object parameters and can measure the system's input-output relationship to derive system disturbance and compensate for its characteristics. The fundamental concept of the disturbance

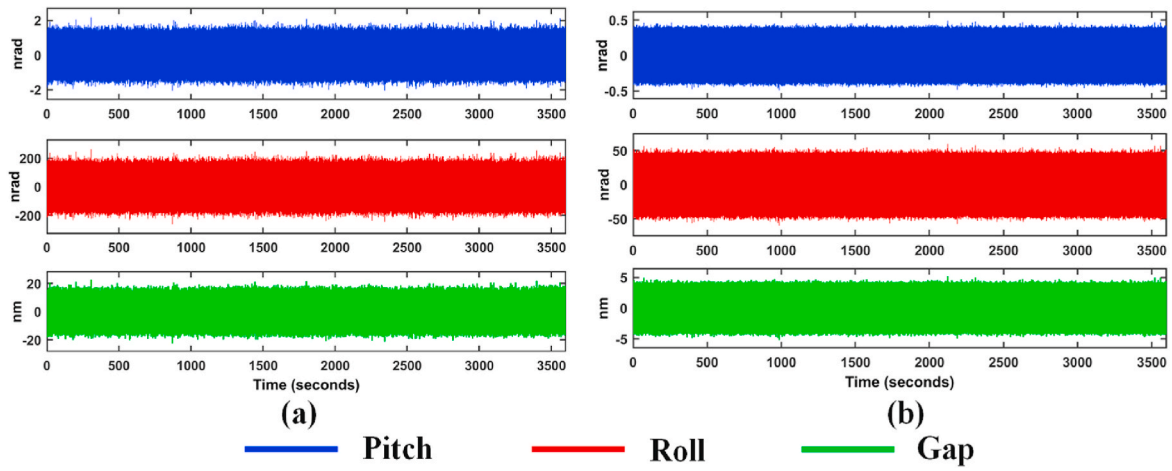

Fig. 18. Stability results of the second crystal with disturbance observer. (a) With disturbance observer. (b) With disturbance observer and phase compensation.

Table 2
Second crystal Pitch/Roll/Gap stability RMS values.

Direction	Without DOB	With DOB	With DOB and PC
Pitch	1.216e+03 nrad	0.3992 nrad	0.1394 nrad
Roll	1.41e+04nad	48.06 nrad	16.61 rad
Gap	1.215e+03 nm	4.412 nm	1.43 nm

observer is that it is designed to detect and mitigate the effects of disturbances. The controlled system output deviates when control inputs are introduced due to disturbances. The observer then compares the control object output to the nominal model output. Equivalent compensation is presented in the control to completely suppress the disturbance caused by the observed difference [23]. The basic schematic of a typical disturbance observer is shown in Fig. 11. $C(s)$ is the controller, $\widehat{d}$ is the disturbance estimate, n is the sensor measurement high frequency noise, $G_n^{-1}(s)$ is the inverse nominal model, $G_0(s)$ is the controlled object model, $G_n(s)$ is the nominal model, and $Q(s)$ is the filter. From the basic principle of Mersenne's formula, the transfer function from u to y is

$$\begin{aligned} G_{uy} &= \frac{G_0(s)}{1-[Q(s)-G_n^{-1}(s)Q(s)G_0(s)]} \\ &= \frac{G_0(s)G_n(s)}{Q(s)G_0(s)+G_n(s)[1-Q(s)]} \\ &= \frac{\dfrac{G_0(s)}{1-Q(s)}}{1+\dfrac{Q(s)G_0(s)}{G_n(s)(1-Q(s))}} \end{aligned} \tag{7}$$

From equation (7) the structure of the disturbance observer can be equated to the system shown in Fig. 12. Therefore, the transfer function from d to y is

$$G_{dy} = \frac{G_0(s)G_n(s)(1-Q(s))}{G_n(s)+[G_0(s)-G_n(s)]Q(s)} \tag{8}$$

The transfer function from n to y is described as

$$G_{ny} = \frac{G_0(s)Q(s)}{G_n(s)+[G_0(s)-G_n(s)]Q(s)} \tag{9}$$

The output y is:

$$y = G_{uy}(s)u + G_{dy}(s)d + G_{ny}(s)n \tag{10}$$

It is crucial to design the filter Q(s) correctly for the disturbance observer, as shown in equations (7)–(9). The central frequency of the interference signal is concentrated in the low-frequency range, while the measurement noise is mainly distributed in the high-frequency range. The design of Q(s) aims to eliminate low-frequency input interference and filter high-frequency noise at the system's output. That is, at low frequencies: $Q(s) = 1, 1/(1-Q(s)) = \infty$, $Q(s)G_n^{-1}(s) = G_n^{-1}(s)$ [24]. In this case, the controlled system is controlled by high gain input. At high frequencies: $Q(s) = 0, 1/(1-Q(s)) = 1$, $Q(s)G_n^{-1}(s) = 0$ [24]. In this case, the disturbance observer does not work in the loop. Therefore, Q(s) is generally designed as a low-pass filter; it can completely suppress low-frequency input disturbances and comprehensively filter high-frequency noise disturbances.

In general, low-pass filters are structured in the form of [25]:

$$Q(s) = \frac{\left[1+\sum_{k=1}^{N-r}\alpha_k(\tau s)^k\right]}{\left[1+\sum_{k=1}^{N}\alpha_k(\tau s)\right]} \tag{11}$$

Where N is the filter order, r is the relative order of the filter; and τ is the time constant.

The larger the filter order, the stronger the immunity, but the computational effort increases and the system stability decreases; to ensure that $Q(s)G_n^{-1}(s)$ can be physically realized, the relative order of the filter should be greater than or equal to the relative order of the system; the smaller the time constant, the more extensive the frequency range of the filter, the stronger the immunity of the system, but the suppression of high frequency noise decreases [26]. The stability adjustment mechanism is a 4th order system with a relative order of 1. The filter design parameters are shown in Table 1, in which case the Bode diagram of Q(s) is shown in Fig. 13. For the stability adjustment mechanism, the primary consideration is the coupling disturbance between the three degrees of freedom and the external disturbance, as well as the computational complexity, is as small as possible, the filter Q(s) is designed as a first-order low-pass filter with time constant ($\tau = 0.001$), and its basic control block diagram is shown in Fig. 14.

The effectiveness of the proposed method is verified based on Simulink. The tracking effect of the system with a sinusoidal signal input of 50 nrad,300Hz (the desired bandwidth of the system) is shown in Fig. 15. Adding a disturbance observer can help the system output closely follow the input. However, there is a small difference in the amplitude and a noticeable delay in the phase of the system. In order to reduce phase angle delay when tracking a 300Hz signal, it is necessary to add a lead controller at 300Hz to compensate for the maximum lead phase angle of the lead link. Let the frequency of the numerator turn of the lead controller be ω_1 and the frequency of the denominator turn be ω_2.The following relationship exists between ω_1 and ω_2 [27]:

$$\omega_1 = 0.1\omega_2 \tag{12}$$

The center frequency of the lead controller is

$$\omega_g = \sqrt{\omega_1 \omega_2} \tag{13}$$

Where $\omega_g = 300$Hz.

The transfer function of the lead controller can be obtained from equations (12) and (13). Fig. 16 shows the tracking effect of the system after phase compensation. It can be seen that the system can eliminate the lag of tracking a 300Hz sinusoidal signal after a steady state after adding the lead controller, which indicates that the lead controller solves the tracking lag problem of the system under 300Hz sinusoidal signal.

The results under the combined disturbance of coupling factor interference, external disturbance, and sensor noise without a disturbance observer are shown in Fig. 17; The stability of the second crystal based on the disturbance observer is shown in Fig. 18; The Pitch/Roll/Gap directional stability RMS/1h metrics are shown in Table 2. By analyzing Fig. 18 and Tables 2 and it can be found that the stability of the second crystal of the DCM in the Pitch/Roll/Gap direction is improved by about 3 orders of magnitude with the disturbance observer; On the other hand, the stability of the second crystal continues to improve by a factor of about 3 or more after the phase compensation. Therefore, the active control method of DCM stability based on disturbance observer can meet current and future beamline engineering requirements.

4. Conclusion

This paper presents a method to design an integral lead compensation notch filter that increases the system bandwidth to 300 Hz and phase margin to 25° by using a dual second-order notch filter with zero-pole pair cancellation based on the root locus method. According to simulation results, using a disturbance observer as a control method significantly improves the stability of the second crystal by suppressing system coupling factor, external disturbances, and high-frequency sensor noise. A phase compensation method using the override controller improves system tracking accuracy with a 50nrad/300Hz sinusoidal input signal. The proposed method in this paper to enhance DCM stability is significant for developing a high-performance DCM for new synchrotron radiation facilities with low emittance and high energy.

Declaration of competing interest

The authors declare that they have no known competing financial interests or personal relationships that could have appeared to influence the work reported in this paper.

Data availability

No data was used for the research described in the article.

Acknowledgments

The work is supported by National Natural Science Foundation of China (No. 61974142, No. 62104224, NO. 62375261) and “Xu-Guang’’ Talent Programof Changchun Institute of Optics, Fine Mechanics and Physics (CIOMP), China, Chinese Academy of Sciences (CAS) (E01672Y6Q0).

References

[1] S. Krinsky, M.L. Penman, R.E. Watson, Characteristics of synchrotron radiation and its sources [M], Handbook on synchrotron radiation 1 (1983). North Holland, Amsterdam, (Chapter 2).
[2] P. Emma, First lasing ofthe LCLS x-ray FEL at 1.5 Å. Particle Accelerator Conference, 2009, p. 3115 (Vancouver BC, Canada).
[3] D.H. Bilderback, P. Elleaume, E. Weckert, Review of third and next generation synchrotron light sources[J], J. Phys. B Atom. Mol. Opt. Phys. 38 (9) (2005) S773.
[4] J. Feldhaus, B. Sonntag, Free-Electron Lasers-High-Intensity X-Ray Sources[J], Springer, New York, 2008.
[5] R. Hettel, DLSR design and plans: an international overview [J], J. Synchrotron Radiat. 21 (5) (2014) 843–855.
[6] C.-L. Li, Research on Large Curvature Arc Vectors Focusing on Double Crystal Monochromators and Related Technology of Multilayer Film Monochromators [D], University of Science and Technology of China, Hefei, 2011, p. 5 (In Chinese).
[7] J. Wu, X. Gong, Y. Song, et al., Improvement of the performance of a cryo-cooled monochromator at SSRF. Part II: angular stability of the exit beam [J], Nucl. Instrum. Methods Phys. Res. Sect. A Accel. Spectrom. Detect. Assoc. Equip. 988 (34) (2021), 164872.
[8] R. Caliari, O. Bagnato, F. Francisco, et al., Studies on Flow-Induced Vibrations for the New High-Dynamics DCM for Sirius [J], 2017.
[9] Y. Fan, H. Qin, W. Zhu, et al., Angular stability measurement of a cry-cooled double-crystal monochromator at SSRF[J], Nucl. Instrum. Methods Phys. Res. Sect. A Accel. Spectrom. Detect. Assoc. Equip. 983 (2020), 164636.
[10] R. Geraldes, et al., Mechatronics Concepts for the New High-Dynamics DCM for Sirius, Sep. 2016 presented at this conference at MEDSI 2016, Barcelona, Spain.
[11] H. Yamazaki, H. Ohashi, Y. Senba, et al., Improvement in stability of SPring-8 X-ray monochromators with cryogenic-cooled silicon crystals[J], J. Phys. Conf. 425 (5) (2013), 052001.
[12] H. Yamazaki, Y. Matsuzaki, Y. Shimizu, et al., Challenges toward 50 nrad-stability of X-rays for a next-generation light source by refining SPring-8 standard monochromator with cryo-cooled Si crystals[C]//AIP Conference Proceedings, AIP Publishing LLC 2054 (1) (2019), 060018.
[13] Jiaxing Wu, Xuepeng Gong, et al., Improvement of the Performance of a Cryo-Cooled Monochromator at SSRF. Part I: Double-Crystal Parallelism [J]. Nuclear Instruments and Methods in Physics Research Section A: Accelerators, Spectrometers, Detectors and Associated Equipment, 2020.
[14] Hongliang Qin, Yichen Fan, Limin Zhang, et al., Design and Stability Performance of a Cradle-type Cryo-Cooled Monochromator at Shanghai Synchrotron Radiation Facility [J]. Nuclear Instruments and Methods in Physics Research Section A: Accelerators, Spectrometers, Detectors and Associated Equipment, 2022.
[15] R.R. Geraldes, R.M. Caliari, G. Moreno, et al., Mechatronics concepts for the new high-dynamics DCM for Sirius [J], SAVE Proc. MEDSI'16 (2016) 44–47.
[16] R.R. Geraldes, G. Witvoet, J. Vermeulen, The mechatronic architecture and design of the High-Dynamic Double-Crystal Monochromator for Sirius light source [J], Precis. Eng. (2022) 77.
[17] R.R. Geraldes, J.L. de Brito Neto, M.S. Silva, et al., A review on the high-dynamic double-crystal monochromator for Sirius/LNLS[C]//Journal of physics: conference series, IOP Publishing 2380 (1) (2022), 012050.
[18] Y. Bai, X. Gong, Q. Lu, et al., Application of adaptive filtering algorithm to the stability problem for double crystal monochromator. Part I: typical filtering algorithms [J], Nucl. Instrum. Methods Phys. Res. Sect. A Accel. Spectrom. Detect. Assoc. Equip. 1048 (2023), 167924.
[19] Y. Bai, X. Gong, Q. Lu, et al., Application of adaptive filtering algorithm to the stability problem for double crystal monochromator. Part II: hybrid algorithms [J], Nucl. Instrum. Methods Phys. Res. Sect. A Accel. Spectrom. Detect. Assoc. Equip. 1046 (2023), 167711.
[20] Y. Bai, X. Gong, Q. Lu, et al., Adaptive vibration control method for double-crystal monochromator based on VMD and FxNLMS [J], J. Synchrotron Radiat. 30 (2) (2023).
[21] C. Hua, Q.G. Wang, X. Guan, Robust adaptive controller design for nonlinear time-delay systems via T-S fuzzy approach[J], IEEE Trans. Fuzzy Syst.: A Publication of the IEEE Neural Networks Council (4) (2009) 17.
[22] G.J. Silva, A. Datta, S.P. Bhattacharyya, On the stability and controller robustness of some popular PID tuning rules[J], IEEE Trans. Automat. Control (9) (2003) 48.
[23] C. Mou, W.U. Qinxian, J. Changsheng, et al., Guaranteed Transient Performance-Based Control with Input Saturation for Near Space vehicles[J], Science China (Information Sciences), 2014.
[24] Yaolun Su, Research on Model Predictive Control Method Based on Perturbation Observer [D], Liaoning University of Petrochemical Technology, 2020 (In Chinese).
[25] H. Shim, N.H. Jo, An almost necessary and sufficient condition for robust stability of closed-loop systems with disturbance observer[J], Automatica 45 (1) (2009) 296–299.
[26] Zhengyun Han, Research on Ship Power Positioning Controller Based on Interference Observer [D], Zhejiang Ocean University, China, 2016 (In Chinese).
[27] Bo Qian, Over Runqiu, Shengli Qu, et al., Principles of Automatic Control [M], Xian University of Electronic Science and Technology Press, China, 2018.